Atmospheric
Chemistry
and Physics

Vertical profiles of black carbon measured by a micro-aethalometer in summer in the North China Plain

Liang Ran[1], Zhaoze Deng[1], Xiaobin Xu[2], Peng Yan[3], Weili Lin[3], Ying Wang[2], Ping Tian[4], Pucai Wang[1], Weilin Pan[1], and Daren Lu[1]

[1]Key Laboratory of Middle Atmosphere and Global Environment Observation, Institute of Atmospheric Physics, Chinese Academy of Sciences, 100029 Beijing, China
[2]Key Laboratory for Atmospheric Chemistry, Institute of Atmospheric Composition, Chinese Academy of Meteorological Sciences, 100081 Beijing, China
[3]Meteorological Observation Center, China Meteorological Administration, 100081 Beijing, China
[4]Beijing Weather Modification Office, 100089 Beijing, China

Correspondence to: Liang Ran (shirleyrl@mail.iap.ac.cn) and Zhaoze Deng (dengzz@mail.iap.ac.cn)

Abstract. Black carbon (BC) is a dominant absorber in the visible spectrum and a potent factor in climatic effects. Vertical profiles of BC were measured using a micro-aethalometer attached to a tethered balloon during the Vertical Observations of trace Gases and Aerosols (VOGA) field campaign, in summer 2014 at a semirural site in the North China Plain (NCP). The diurnal cycle of BC vertical distributions following the evolution of the mixing layer (ML) was investigated for the first time in the NCP region. Statistical parameters including identified mixing height (H_m) and average BC mass concentrations within the ML (C_m) and in the free troposphere (C_f) were obtained for a selected dataset of 67 vertical profiles. H_m was usually lower than 0.2 km in the early morning and rapidly rose thereafter due to strengthened turbulence. The maximum height of the ML was reached in the late afternoon. The top of a full developed ML exceeded 1 km on sunny days in summer, while it stayed much lower on cloudy days. The sunset triggered the collapse of the ML, and a stable nocturnal boundary layer (NBL) gradually formed. Accordingly, the highest level C_m was found in the early morning and the lowest was found in the afternoon. In the daytime, BC was almost uniformly distributed within the ML and significantly decreased above the ML. During the field campaign, C_m averaged about $5.16 \pm 2.49\,\mu g\,m^{-3}$, with a range of 1.12 to $14.49\,\mu g\,m^{-3}$, comparable with observational results in many polluted urban areas such as Milan in Italy and Shanghai in China. As evening approached, BC gradually built up near the surface and exponentially declined with height. In contrast to the large variability found both in H_m and C_m, C_f stayed relatively unaffected through the day. C_f was less than 10 % of the ground level under clean conditions, while it amounted to half of the ground level in some polluted cases. In situ measurements of BC vertical profiles would hopefully have an important implication for accurately estimating direct radiative forcing by BC and improving the retrieval of aerosol optical properties by remote sensing in this region.

1 Introduction

Black carbon (BC), produced from incomplete combustion processes, is a strongly absorbing constituent of atmospheric aerosols (Moosmüller et al., 2009; Bond et al., 2013). As a major absorber in the visible spectrum, BC heats the atmosphere and largely counterbalances cooling effects of scattering aerosols on climate (Jacobson, 2001; Ramanathan et al., 2005; Stier et al., 2007). Another reason for BC to be of public concern is that inhaled BC poses a huge threat to human health (Janssen et al., 2012; Nichols, 2013).

Despite the significance of evaluating radiative forcing by BC, large uncertainties arise from limitations of current knowledge on emissions, distributions, and physical properties of BC (Andreae, 2001; Streets, et al., 2001; Bond et al.,

2006; IPCC, 2013). One critical aspect pertinent to climate response of BC is a high sensitivity of BC radiative impact to its vertical distributions (Zarzycki and Bond, 2010; Ban-Weiss et al., 2012; Samset et al., 2013). The importance of BC vertical distributions to the evolution of planetary boundary layer (PBL) and cloud properties has also been demonstrated by previous studies (Yu et al., 2002; Ramanathan and Carmichael, 2008; Ferrero et al., 2014). Nevertheless, vertical profiles of BC or aerosol absorption have only been scarcely measured in a few field campaigns (Safai et al., 2012 and references therein; Ryerson et al., 2013). Available information on BC vertical distributions is particularly limited in China (Zhang et al., 2012; Li et al., 2015; Zhao et al., 2015), issuing a challenge to reliably estimate regional climatic effects of BC under severe air pollution due to rapid economic growth and urbanization in this region (Menon et al., 2002; Liao and Shang, 2015 and references therein).

Platforms normally utilized to perform BC profiling are tethered balloons, aircraft, and unmanned aerial vehicles. BC vertical profiles obtained from in situ measurements using tethered balloons are highly vertically resolved, revealing details within about 1 km above the ground, especially in the thin surface layer that is vital for human beings and where various sources are located (Ferrero et al., 2011a; Babu et al., 2011a; Li et al., 2015). Comparatively, aircraft (Tripathi et al., 2005, 2007; Metcalf et al., 2012; Zhao et al., 2015) and unmanned aerial vehicles (Corrigan et al., 2008; Höpner et al., 2016) are more expensive, although they have advantages of reaching higher altitudes and for aircraft, more on-board instruments of the size and weight unable to be carried by tethered balloons and unmanned aerial vehicles. Fast flight speeds of these two platforms also compromise their spatial resolutions. In addition, a high-altitude balloon has been employed to measure BC vertical profiles at high altitudes in the free troposphere. Two BC polluted layers found at about 4.5 and 8 km altitudes were reported by Babu et al. (2011b). Indirect methods such as recently proposed lidar remote sensing might be able to conduct continuous measurements (Miffre et al., 2015). They are, however, less accurate than in situ measurements.

To advance understanding in impacts of atmospheric components including trace gases and aerosols on atmospheric environment and climate, an intensive field campaign, Vertical Observations of trace Gases and Aerosols (VOGA), was carried out in summer 2014 at a semirural site in the North China Plain (NCP), one of the most overcrowded and polluted regions in the world (Shao et al., 2006; Xu et al., 2011; Ma et al., 2011; Chen et al., 2012). A tethered balloon system equipped with instruments was employed for high vertical resolution measurements within 1 km above the ground. In this study, we present results from in situ measurements of BC vertical profiles using a lightweight (about 280 g) and small-sized (117 mm × 66 mm × 38 mm) micro-aethalometer (microAeth® Model AE-51, Magee Scientific,

USA). The diurnal cycle of BC vertical distributions was explored for the first time in the NCP region.

2 Experiment

2.1 The site

The VOGA 2014 field campaign was carried out in the period from 21 June to 14 July at a semirural site, Raoyang (38°14′ N, 115°44′ E, 20 m a.s.l.), about 50 km north of the city of Hengshui in the central NCP (Fig. 1). The county of Raoyang, in which the site is located, is less industrialized and relies mainly on agriculture, but is surrounded by a cluster of industrial and populated cities within a distance of 100 km, and respectively about 190 and 160 km southwest of the twin megacities of Beijing and Tianjin.

The spatial distribution of average aerosol optical depth (AOD) at 550 nm acquired from the level 2 version of the Moderate Resolution Imaging Spectroradiometer (MODIS) data (Levy and Hsu, 2015) is also displayed in Fig. 1. Features of severe regional aerosol pollution with clearly defined pollution centers could be recognized from the AOD distributions in different months of the year 2014. The level of AOD in Raoyang could represent regional aerosol conditions in NCP in July 2014 well, the month when most tethered balloon flights took place (Fig. 1c). The AOD distributions could also cast some light on the seasonal variation of ambient aerosols in the area where launches of the tethered balloon were carried out, since measurements of absorbing aerosols are unavailable to obtain the temporal variation in that area. However, it should be noted that the seasonal cycle of ambient aerosols depends on both the aerosol loading and the relative humidity. As a consequence, it is complicated to draw a definite conclusion only from the AOD dataset about to what extent reported BC concentrations in this study represent the spatiotemporal variability in the area. A further examination on BC emissions (0.25° × 0.25°) from four sectors (industry, power, residential activity, and transportation) in 2012 in the NCP region was performed on the basis of emission data generated from the multi-resolution emission inventory for China (MEIC, http://www.meicmodel.org) model (Li et al., 2015), which is developed by a technology-based approach (Lei et al., 2011). It could also tell from the emission inventory of BC that aerosol conditions at the site of Raoyang represents the regional situation well, with influences from several nearby emission centers (Fig. S1 in the Supplement).

Moreover, it was found that another semirural site Gucheng, about 90 km north of Raoyang, shared a similarity with Raoyang in the AOD level as well as BC emissions. Seasonal and diurnal variations of surface BC mass concentrations in Gucheng were analyzed on the basis of about 6-year measurements (from 2006 January to July 2012, with data completeness of 77.5 %) using an aethalometer (Model
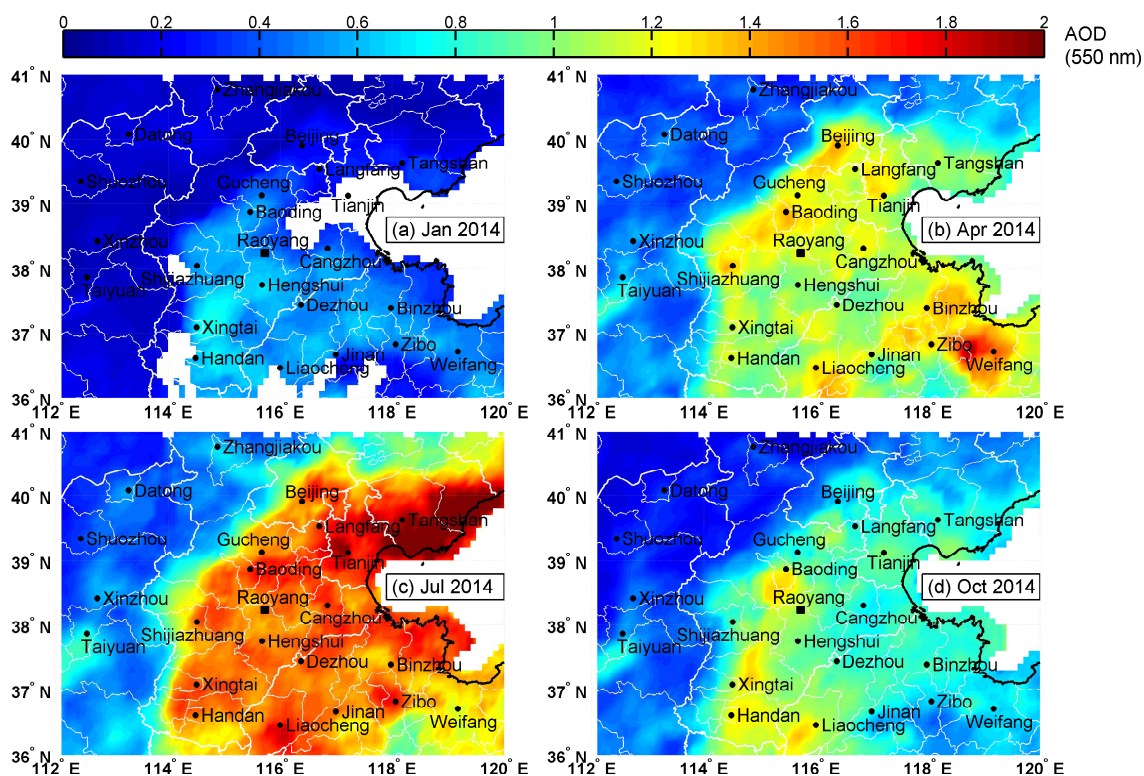
Figure 1. The spatial distribution of averaged MODIS aerosol optical depth (AOD) at 550 nm in **(a)** January; **(b)** April; **(c)** July; **(d)** October 2014 in the NCP. The locations of the semirural site Raoyang and major cities are respectively marked by a square and dots. Only grids with the fraction of valid data exceeding 30 % in the month are shown.

AE-31, Magee Scientific, USA) with a temporal resolution of 5 min (Zhang et al., 2015). BC mass concentrations averaged about $9.6 \pm 8.4\,\mu\mathrm{g\,m^{-3}}$ during 2006 and 2012 in Gucheng, with a lower level in summer and spring. The diurnal cycle of BC mass concentrations indicated higher values at night and a low valley in the afternoon. Thus, it might be expected that BC mass concentrations measured in summer at Raoyang were probably lower than that in other seasons.

2.2 Instruments

A micro-aethalometer to measure aerosol absorption at 880 nm and a radiosonde to measure meteorological parameters (pressure, temperature, relative humidity, wind speed, and wind direction) were attached to a helium-filled tethered balloon, with a volume of 30 m^3 and a payload weight of 10 kg. The fish-shaped balloon was well balanced during launches; thus the disturbance imposed on instruments by ascents and descents of the balloon could be largely minimized. Launches were scheduled every 3 h between 06:00 and 21:00 local time (LT) from the ground to 1 km height. However, feasible launches actually depended upon wind speed and precipitation, as well as air traffic control. In total, 48 successful launches were conducted in 15 days, of which 40 reached above 0.5 km. Through the entire field campaign,

89 vertical profiles of BC were reliably obtained. Lack of data for several ascending or descending processes was primarily caused by discarding invalid data under wind gusts, which led to the violent swing of the tethered balloon and poor data quality. The balloon ascended at a rate of $1\,\mathrm{m\,s^{-1}}$ and descended at a rate of $0.5\,\mathrm{m\,s^{-1}}$ under the control of an electric winch. With a sampling interval of 1 s for all instruments, the observational vertical resolution was ~ 1 m. For analysis in this study, 20 m averaged data were used.

AE-51 operated with a similar principle to the aethalometer as described in Hansen et al. (1984). The intensity of transmitted light through a 3 mm diameter sample spot (I) and an aerosol-free reference spot (I_0) on a T60 Teflon-coated borosilicate glass fiber filter were simultaneously detected to obtain attenuation coefficients at the wavelength of 880 nm ($\sigma_{\mathrm{AE-51,\,880\,nm}}$), following

$$\sigma_{\mathrm{AE-51,\,880\,nm}} = \frac{A \times \Delta\mathrm{ATN}}{100 \times F \times \Delta t},\qquad(1)$$

where A is the area of the aerosol collecting spot (0.071 cm^2), F is the flow rate (150 mL min^{-1}), ATN denotes light attenuation calculated from $100 \times \ln(I_0/I)$, and $\Delta\mathrm{ATN}$ is the change of ATN during the sampling interval Δt (1 s). A homemade silica gel dryer was placed in front of the inlet to efficiently dry ambient aerosols. A test on the dryer

was performed before the campaign to ensure the duration and efficiency of its usage.

2.3 Data processing

2.3.1 The smoothing algorithm

At a high temporal resolution of 1 s, a steady increase of ATN with sampling time was not usually found due to instrumental noise. Acquired data consisted of many large values with positive or negative signs. A post-processing method, the Optimized Noise-reduction Averaging (ONA) algorithm, has been developed by Hagler et al. (2011), where adaptive time-averaging of the BC data was conducted with the time window of averaging optimally chosen by ΔATN. In this study, data dispersion due to high temporal resolution was treated by a new smoothing algorithm, Fluctuation Minimizing Smoothing (FMS). Similar to the ONA method, the FMS approach is also principally based upon the physical behavior of measured ATN. Despite the fact that BC values determined from fluctuated ATN might vary drastically, large positive/negative pairs of BC values would always be found and counterbalance each other within a few seconds. Therefore, the FMS approach was devised to find pairs of BC values that differ largely from each other within a few seconds and make a compromise. The procedure was performed as follows.

1. For each data point x_i of a continuously measured time series with N records, calculate the difference between x_i and all other data points within n seconds to generate a matrix of $\mathbf{D}_{i,j} = |x_i - x_{i+j}|$, where $i = 1, 2, \ldots, N-1$, N and $j = 1, 2, \ldots, n-1, n$.

2. Find the largest value of the matrix $\mathbf{D}_{k,l}$, which is the difference between point x_k and x_{k+l}.

3. Replace x_k and x_{k+l} with $(x_k + x_{k+l})/2$ and set $\mathbf{D}_{k,l}$ to a minus number.

4. Replace any $\mathbf{D}_{i,j}$ that has been calculated using x_k or x_{k+l}, except for $\mathbf{D}_{i,j}$ with a minus number. This step is optional, since it largely raises the computational cost.

5. Repeat step 2–4 until there are no positive numbers in the matrix.

6. Repeat step 1–5 for m times to obtain acceptable smoothed data.

The smoothing window n and the smoothing count m were empirically chosen during the calculation. It should be kept in mind that using improper large n or m might wipe off some natural variations, although it will always give a smoother result. n should be set to no more than 5, given that data fluctuation is normally already compensated within 5 s. With n to be 5 and m to be 1, the average of the target point was mostly contributed from neighboring data points within about 11 s, according to a weight of 80 %. This consequently led to a

vertical resolution of about 22 m for the ascent and 11 m for the descent after smoothing. Similarly, the vertical resolution was about 50–60 m for the ascent and 25–30 m for the descent when m was set to be 5. Different choices of m gave a similar pattern of vertical profiles, but with some differences in details. In this study, m was set to be 5 to achieve a better smoothing for further calculations, though this caused a loss of the vertical resolution more than twice as large as that when just smoothing once. A comparison was made between unsmoothed data, smoothed data using the FMS approach in this study, and the ONA method in Hagler et al. (2011), as well as 20 m averaged data using those two algorithms. It was found that both algorithms could properly deal with data fluctuation caused by instrumental noise without introducing artificial features (e.g., Fig. 3a–c). However, the FMS method seemed to be more capable of reliably removing outliers in some cases (e.g., Fig. 3d–f). The comparison indicated that the FMS procedure could effectively reduce data fluctuation while still preserve reasonable variability of the profile.

2.3.2 The correction method

Measured $\sigma_{AE-51, 880\,nm}$ suffered from systematic biases introduced by the filter-based technique. In order to determine BC absorption coefficients (σ_{BC}) from $\sigma_{AE-51, 880\,nm}$, correction was required to tackle three types of artifacts. The shadowing effect, an artifact that results in gradual artificial reduction in $\sigma_{AE-51, 880\,nm}$ due to the saturation of the filter with increasing aerosol loading, leads to an underestimation of σ_{BC} and a discontinuity after changing to a new sample spot (Weingartner et al., 2003). Various methods have been developed to address the shadowing effect (Weingartner et al., 2003; Virkkula et al., 2007; Ran et al., 2016). However, this artifact could be neglected in this study, since no ATN exceeded 20 with a new filter for each launch. The other two artifacts cause an overestimation of σ_{BC} by enhancing light attenuation, either due to aerosol scattering or the multiple scattering of filter fibers (Weingartner et al., 2003; Arnott et al., 2005; Schmid et al., 2006; Collaud Coen et al., 2010). A correction factor (C) was needed to correct these two artifacts.

The C factor was derived from a surface comparative test for about 1 week in Beijing between AE-51, a 7-wavelength aethalometer (Model AE-31, Magee Scientific, USA) and a multi-angle absorption photometer (MAAP, Model 5012, Thermo, USA). Continuous operation of AE-51 was carried out in order to obtain a proper size of the dataset in a limited time period, despite the fact that AE-51 is, in principle, not designed to be operated around the clock. A daily check of the flow rate was performed using a Gilibrator-2 Diagnostic Kit (Sensidyne, USA) to ensure the stability of the flow and thus data quality.

AE-31 suffered instrumental artifacts in the same way as AE-51. Details of the correction scheme developed for tackling AE-31 artifacts were described in Ran et

al. (2016). Briefly, the correction scheme combined the modified Virkkula method (Virkkula et al., 2007) to treat the shadowing effect and the Schmid method (Schmid et al., 2006) to treat filter multiple scattering and aerosol scattering effects. The modified Virkkula method assumed a linear relationship of BC mass concentrations and time across the filter change, particularly, a quadratic relationship for special cases where ambient BC experienced a peak-shaped variation, instead of constant BC mass concentrations as in Virkkula et al. (2007). The wavelength-dependent correction factor (C_λ) could be obtained following procedures in Schmid et al. (2006). The temporal resolution of AE-31 during the comparative test was 2 min.

MAAP continuously measured aerosol absorption coefficients at the actual wavelength of 637 nm ($\sigma_{MAAP, 637\,nm}$) instead of the nominal wavelength of 670 nm (Müller et al., 2011), with a temporal resolution of 1 min. Multi-angle detections of the transmittance and reflectance, as well as a two-stream approximation in the radiative transfer scheme adopted by MAAP, have significantly improved measurements of ambient aerosol absorption coefficients (Petzold and Schönlinner, 2004; Petzold et al., 2005). Hyvärinen et al. (2013) reported an artifact of underestimated BC mass concentrations after a spot change and attributed it to yet unconfirmed causes as erroneous dark counts in the transmitted light photodetector and an instrument internal averaging procedure of the photodetector raw signals. It was stated that this artifact could be observed with a BC mass accumulation rate, as the product of BC mass concentrations and the flow rate of MAAP, larger than $0.04\,\mu g\,min^{-1}$, which corresponds to $3\,\mu g\,m^{-3}$ at the flow rate of $1\,m^3\,h^{-1}$. However, no apparent underestimation of BC mass concentrations was found in this study, even for cases where BC mass concentrations exceeded $8\,\mu g\,m^{-3}$ (Fig. S2). Consequently, measured $\sigma_{MAAP, 637\,nm}$ without any correction was used for subsequent calculations and taken as real values.

Three steps were taken to obtain the C factor. Firstly, aerosol absorption Ångström exponent (α) over the spectrum span of 660 and 880 nm was derived from absorption coefficients $\sigma_{AE-31, 660\,nm}$ and $\sigma_{AE-31, 880\,nm}$, which were corrected from attenuation coefficients at 660 and 880 nm measured by AE-31. Hence, α was calculated from

$$\alpha = \frac{\ln(\sigma_{AE-31, 660\,nm}) - \ln(\sigma_{AE-31, 880\,nm})}{\ln(880) - \ln(660)}. \tag{2}$$

Secondly, α for the spectrum of 660 and 880 nm was used to represent α over the span of 637 and 880 nm. Therefore, $\sigma_{MAAP, 880\,nm}$ was quantified from measured $\sigma_{MAAP, 637\,nm}$ following the spectral dependence of aerosol absorption coefficients in the form of $\lambda^{-\alpha}$:

$$\sigma_{MAAP, 880\,nm} = \sigma_{MAAP, 637\,nm} \times \left(\frac{880}{637}\right)^{-\alpha}. \tag{3}$$

Finally, reduced major axis regression of attenuation coefficients $\sigma_{AE-51, 880\,nm}$ (ATN < 10) measured by AE-51 and ab-

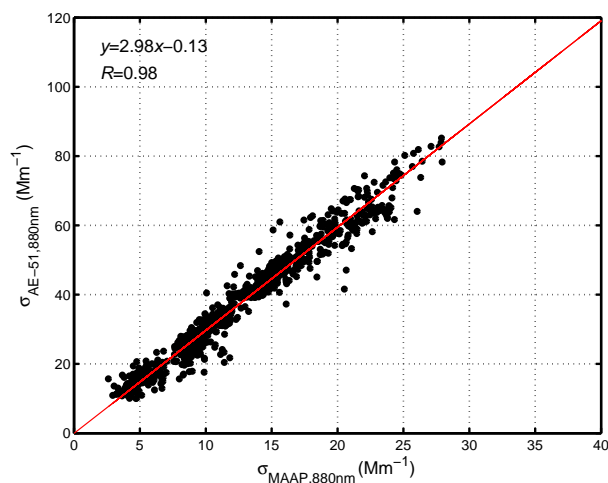**Figure 2.** Reduced major axis regression of attenuation coefficients $\sigma_{AE-51, 880\,nm}$ (ATN < 10) measured by AE-51 and absorption coefficients $\sigma_{880\,nm}$ calculated from concomitant MAAP and AE-31 measurements in the comparative test.

sorption coefficients $\sigma_{MAAP, 880\,nm}$ calculated from MAAP and AE-31 yielded the C factor of 2.98 ± 0.05 with 95 % confidence (Fig. 2). It is noted that the C factor for AE-51 was reported as 2.05 ± 0.03 with 95 % confidence in Ferrero et al. (2011a). Possible explanations on such a difference in the C factor might be found in aerosol chemical compositions in the NCP region and the Po Valley basin. Besides, the C factor in Ferrero et al. (2011a) was obtained from Mie calculations, and thus was subject to uncertainties resulting from assumptions such as BC size distributions, BC mixing state, and particle morphology. In addition, the choice of the correction scheme for AE-31 measurements in this study might introduce uncertainties to α and thereby $\sigma_{MAAP, 880\,nm}$. Using a constant C factor for AE-31 as also often used in some studies (e.g., Weingartner et al., 2003; Sandradewi et al., 2008) instead of the wavelength-dependent C_λ results in an underestimation of α over the 660–880 nm spectrum by about 19.5 %. This consequently leads to an overestimation of $\sigma_{MAAP, 880\,nm}$ and the C factor for AE-51 by about 9.6 and 8.4 %, respectively. By dividing C into $\sigma_{AE-51, 880\,nm}$, absorption coefficients σ_{BC} could be estimated. As for the mass concentration of BC (m_{BC}), it could be directly converted from $\sigma_{AE-51, 880\,nm}$ using the documented "specific attenuation" of $12.5\,m^2\,g^{-1}$, considering that BC is the major contributor to aerosol absorption at 880 nm (Ramachandran and Rajesh, 2007).

2.3.3 The calculation of meteorological parameters

Instead of measured temperature (T) and relative humidity (RH), two conservative quantities, potential temperature (θ) and specific humidity (q), were used to provide information on the evolution of the PBL. The calculation of θ (K) fol-

lowed

$$\theta = T \times (p_0/p)^{R_d/C_{pd}}, \tag{4}$$

where p and p_0 are measured pressure and the standard pressure at sea level (hPa) respectively, T is measured temperature (K), R_d is the individual gas constant for dry air ($287\,\mathrm{J\,kg^{-1}\,K^{-1}}$), and C_{pd} is the specific heat at constant pressure for dry air at the standard temperature ($1005\,\mathrm{J\,kg^{-1}\,K^{-1}}$). Calculated θ was then expressed in degree Celsius (°C) in order to be straightforward. Specific humidity (q, $\mathrm{g\,kg^{-1}}$) was calculated from

$$q = \varepsilon \times \frac{e}{p - (1-\varepsilon) \times e} \times 1000, \tag{5}$$

where ε is the ratio of the molecular weight of water vapor to that of dry air (0.622) and e is the vapor pressure of water (hPa), which is the product of measured RH (%) and calculated water saturation pressure (e_s) at each measured temperature T.

3 Results and discussion

3.1 Vertical distributions of BC and meteorological parameters

A set of 67 vertical profiles of BC and meteorological parameters were selected. The mixing layer (ML) could be clearly discerned for profiles measured in the daytime. Exceptions were those measured around noon, when the top of the ML, often higher than 1 km in summer, was beyond reach of the tethered balloon. In addition, several launches took place in the evening to observe BC vertical distributions shaped by the nocturnal boundary layer (NBL). A statistical summary of the field campaign and the meteorology is given in Table 1. Most profiles were sampled under mild winds in the morning and evening, when relatively stable conditions suitable for launches of the tethered balloon were more easily encountered. Air masses were mainly carried, either by southeasterly or southwesterly winds, from areas densely populated and heavily industrialized, also ramified with railways and highways.

Figure 4 illustrates an example of vertical distributions of BC, θ, q, and winds during one launch on 8 July 2014 (10:41–11:27 LT). The 20 m averaged data are denoted by dots in dark color for the ascent and light color for the descent. Arrows depict vector mean horizontal winds, with the length representing wind speed and the arrowhead giving wind direction following meteorological definitions. The height of a clearly defined ML was marked by a solid line for each BC vertical profile. A nearly uniform distribution of BC, as well as θ and q, was observed within the strongly convective ML. A large vertical gradient of m_{BC} across the entrainment layer (EL) led to approximately 50 % reduction from the level in the ML to that in the free troposphere (FT).
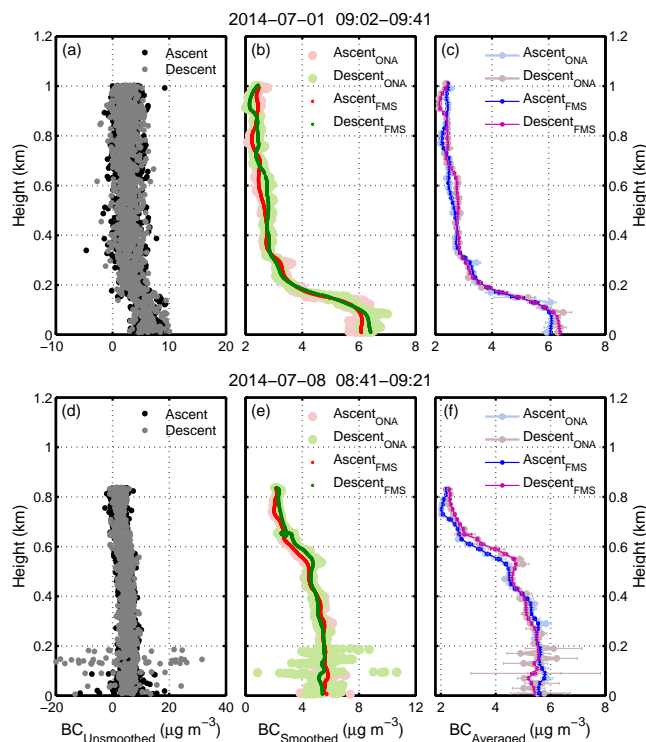

Figure 3. (a) Unsmoothed BC mass concentrations measured with a temporal resolution of 1 s on 1 July 2014 (09:02–09:41 LT). Data points collected from the ascending and descending process are respectively marked in black and gray dots. (b) Smoothed BC mass concentrations using two algorithms. Data points processed by the ONA method are displayed in large pink dots for the ascent and in light green for the descent. Data points processed by the FMS method are denoted by small red dots for the ascent and green dots for the descent. (c) 20 m averaged profiles based upon smoothed data using two algorithms. Dots indicate 20 m averages, with standard deviations in error bars. Results from the ONA and FMS methods are respectively given in light blue and blue for the ascent, while in light purple and purple for the descent. (d–f) Measured and processed BC vertical profiles on 8 July 2014 (08:41–09:21 LT). The caption is the same as that in (a)–(c).

Concomitantly, a substantial reduction in q, whereas an increase in θ, was also immediately found above the ML. The difference in profiles between the ascent and the descent evidently indicated a rapid evolution of the ML near noon and its impact on vertical distributions of BC and meteorology. More discussions regarding diurnal variations of BC vertical profiles can be found in the next section.

The mixing height could be determined by applying the gradient method to the entire dataset (Seibert et al., 2000; Kim et al., 2007). Generally, the mixing height determined from profiles of m_{BC} ($H_{m,BC,gradient}$) agreed well with that from profiles of θ ($H_{m,\theta}$) and q ($H_{m,q}$) as shown in Fig. S3. The reliability of estimating the mixing height from vertical measurements of BC had also been demonstrated in previous studies (Ferrero et al., 2010; Ferrero et al., 2011b). On the

Table 1. A statistical summary of the field campaign and the meteorology. H_{max} denotes the maximum height reached by the tethered balloon. $T_{10\,m}$, $RH_{10\,m}$, and $WS_{10\,m}$ indicated temperature, relative humidity, and wind speed within 10 m near the surface, in the form of average value $\pm$ standard deviation. $WD_{10\,m}$ represents frequently encountered wind direction. The last column gives the weather that mostly occurred during each period.

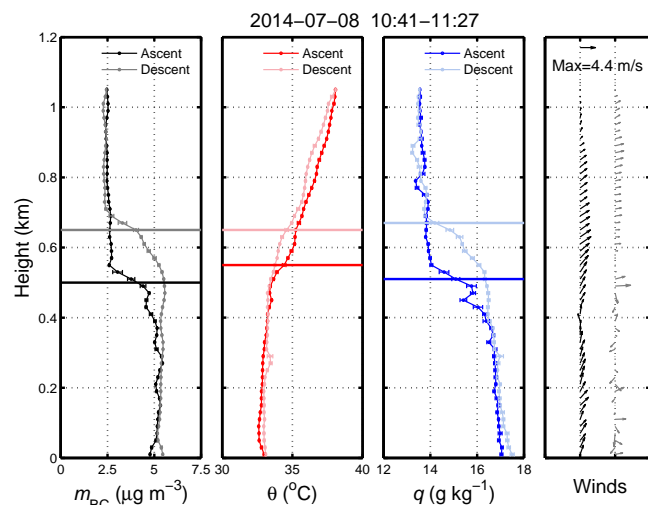| Periods	Profiles	H_{max} (km)	$T_{10\,m}$ (°C)	$RH_{10\,m}$ (%)	$WS_{10\,m}$ (m s^{-1})	$WD_{10\,m}$	Weather
06:00–09:00	23	0.28–0.92	25.3 ± 0.8	62.7 ± 3.2	2.9 ± 1.3	Southwest	Cloudy
09:00–12:00	20	0.32–1.06	26.0 ± 1.5	61.0 ± 3.4	2.6 ± 1.1	Southwest	Cloudy
12:00–15:00	4	0.84–1.14	28.7 ± 2.3	55.9 ± 5.0	2.2 ± 1.4	Southeast	Fine
15:00–18:00	6	1.04–1.08	28.5 ± 2.4	58.7 ± 4.6	2.1 ± 1.1	Southeast	Fine
18:00–21:00	14	0.26–1.16	29.1 ± 2.2	45.0 ± 3.3	1.8 ± 0.8	Southwest	Fine

Figure 4. Vertical profiles of BC mass concentrations (m_{BC}), potential temperature (θ), specific humidity (q), and winds on 8 July 2014 (10:41–11:27 LT). Profiles measured during the ascent are displayed in dark colors, while those during the descent are displayed in light colors. Dots indicate 20 m averaged data, with standard deviations in error bars. Heights of the mixing layer (ML) estimated from vertical profiles are given in horizontal lines. Arrows show vector mean horizontal winds, with northerly winds indicated by downward arrows. The wind vector for the maximum wind speed is marked by the text label.

other hand, typical daytime profiles of m_{BC} could be well characterized by the sigmoid function

$$m_{BC} = C_{ms} - \frac{C_{ms} - C_{fs}}{e^{-(h-H_{m,BC,sigmoid})/H_e} + 1}, \quad (6)$$

where C_{ms} and C_{fs} are characteristic m_{BC} within the ML and in the FT respectively, $H_{m,\,BC,\,sigmoid}$ is the mixing height derived from BC vertical profiles using the sigmoid function, H_e represents the thickness of the EL, and h is the height at which each 20 m averaged m_{BC} is obtained. The parameters C_{ms}, C_{fs}, $H_{m,\,BC,\,sigmoid}$, and H_e could be directly determined by fitting measured m_{BC} at each height h using Eq. (6) as shown by the example (Fig. S4). A comparison was made between $H_{m,\,BC,\,gradient}$ and $H_{m,\,BC,\,sigmoid}$ for typ-

ical daytime BC vertical profiles. Results from the two methods agreed quite well with each other, with a difference of less than 2 % (Fig. S5). In addition to reliably estimating the mixing height as the gradient method, the sigmoid function could also directly determine parameters including C_{ms}, C_{fs}, and H_e. Therefore, the sigmoid function was chosen to obtain all parameters for typical daytime BC profiles. As for non-typical daytime BC profiles, either as a result of a polluted layer in the FT or barely sufficient height into the FT reached by the tethered balloon, a sigmoid function was not applicable and the gradient method was used to estimate the mixing height. Near sunset, the NBL forms along with the collapse of the ML (Kaimal and Finnigan, 1994; Lazaridis, 2011). The structure of the NBL is more complicated and the determination of the NBL height bears more uncertainty (Yu, 1978; Poulos, et al., 2002). A subjective procedure based on the gradient method was utilized to estimate the NBL height. In summary, the mixing height determined from vertical profiles of BC, either by the gradient method or the sigmoid function, as well as the estimated NBL height, were denoted as H_m in this study for convenience.

Table 2 summarizes calculated parameters for BC vertical profiles during different periods. Average m_{BC} within the ML and in the FT were denoted as C_m and C_f, which were C_{ms} and C_{fs} for typical daytime BC profiles. As for non-typical daytime BC profiles, C_m was the average of m_{BC} below H_m. When H_m exceeded 1 km, m_{BC} measured along the ascending/descending path from the ground to the maximum height reached by the tethered balloon were averaged to obtain C_m. For NBL cases, only C_f was obtained, by averaging m_{BC} above H_m. A large variability was found in C_m, with a range of 1.12 to 14.49 µg m^{-3}. On average, C_f stayed relatively steady; though it ranged from 0.36 µg m^{-3} in clean cases to 3.14 µg m^{-3} under polluted conditions.

Statistically, vertical profiles of BC were categorized into two types, according to their shapes along the normalized height (H_{Nor}), which was calculated from $h/H_m - 1$ (Ferrero et al., 2014). H_{Nor} shows the surface with a value of -1 and the top of the ML with a value of 0. One type of BC vertical profiles, exclusively measured in the daytime, displayed a vertical distribution typically shaped by a well-mixed mixing

Table 2. Statistical parameters for BC vertical profiles measured during different periods. Notations for the parameters have been given in the text.

Parameters	06:00–09:00 23 profiles	09:00–12:00 20 profiles	12:00–15:00 4 profiles	15:00–18:00 6 profiles	18:00–21:00 14 profiles
H_m (km)	0.08–0.29	0.18–0.87	0.43–1.14	0.69–1.08	0.19–0.25
H_e (km)	0.05–0.04	0.05–0.03			
C_m (µg m^{-3})	3.1–14.49 (6.61 ± 2.93)	2.56–5.80 (4.42 ± 1.11)	1.12–6.15 (3.77 ± 2.06)	2.04–4.11 (3.05 ± 0.86)	
C_f (µg m^{-3})	0.46–3.14 (1.67 ± 0.95)	0.41–2.51 (1.77 ± 0.75)			0.36–2.83 (1.36 ± 1.12)

layer (Fig. 5a). BC was almost uniformly distributed within the ML, in a similar way to the example (Fig. 4), with an average m_{BC} level of about $5.16 \pm 2.49 \, \mu g \, m^{-3}$, or σ_{BC} of about $21.64 \pm 10.45 \, Mm^{-1}$. This is comparable with what has been observed within the PBL in many polluted urban areas (Table 3). A couple of highly polluted cases, where C_m exceeded $10 \, \mu g \, m^{-3}$, were observed in the early morning. The formation of the convective ML just started at that time and vertical turbulence was not yet strong enough to dilute the high level of BC, which was primarily emitted near the ground and accumulated within the stable NBL over night. Due to a sharp reduction in m_{BC} from the ML to the FT, average C_f was about $1.61 \pm 0.94 \, \mu g \, m^{-3}$. The second type of BC vertical profiles revealed the feature of trapped air pollutants in the shallow stable NBL. For each BC profile (gray lines in Fig. 5b), m_{BC} nearly exponentially declined with H_{Nor}, as a result of weakened turbulence and vertical dispersion. Under polluted conditions, C_f could reach as high as $2.83 \, \mu g \, m^{-3}$, otherwise usually well below $1 \, \mu g \, m^{-3}$.

3.2 Diurnal variations of BC vertical profiles

An investigation on diurnal variations of BC vertical profiles was able to be undertaken on 1, 8, and 13 July, when measurements generally covered the period from early morning to afternoon or evening. On other observational days, the dataset was incomplete due to aborted launches under strong winds or precipitation. For clarity, only the vertical profile during the descent of each launch is plotted in Fig. 6. Additionally, profiles not included in the selected dataset are also shown.

A distinct diurnal variation was found both in the shape of BC vertical profiles and the level of m_{BC} along the profile. To a great extent, the diurnal cycle of BC vertical profiles followed the evolution of the ML. In the early morning, BC was largely restricted within a thin ML less than 0.2 km above the ground when vertical turbulence was still weak. m_{BC} dropped dramatically from a high level within the ML to a significantly low level above the ML, even less than 10 % as could be found on 13 July. In polluted cases, however, m_{BC} in the FT could exceed $2 \, \mu g \, m^{-3}$ and sometimes reach nearly 50 % of that at the surface (e.g., profiles
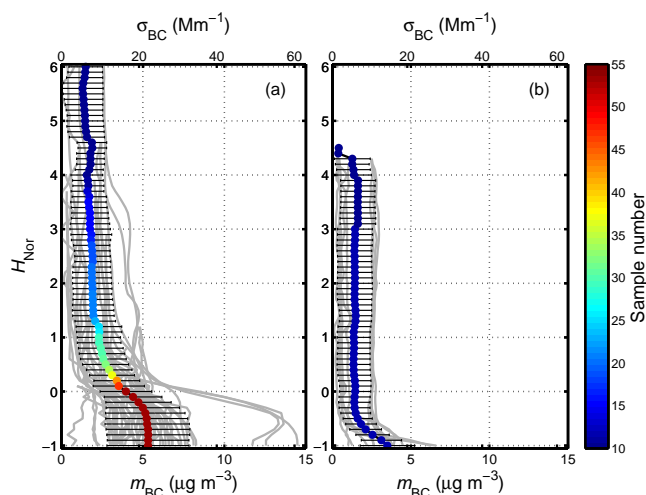

Figure 5. Vertical distributions of m_{BC} (bottom axis) and σ_{BC} (top axis) along the normalized height H_{Nor} **(a)** in the daytime and **(b)** in the evening during the field campaign (gray lines). The average profile is shown by the black line, with error bars representing standard deviations. Average values are indicated by dots, with the color showing the number of samples at each layer.

on 1 and 8 July). This might imply the existence of a polluted residual layer above the stable surface layer formed after the sunset in previous evening; yet this is unable to be discussed further without continuous measurements from the day before. The characteristics of m_{BC} in the FT should also be affected by the advection. After sunrise, vertical turbulence in the ML gradually strengthened as the earth was continuously heated by solar radiation. The convective ML developed quickly in the forenoon, with elevated H_m and decreased C_m. Marked changes in BC vertical profiles could be observed even during one launch when the mixing height rose so rapidly, as shown in the example (Fig. 4). The maximum height of the ML commonly exceeded 1 km in the afternoon during the field campaign (e.g., profiles on 8 July), except on cloudy days when the ML did not fully develop. As the evening approached, convection abruptly decayed and a stable NBL began to form. m_{BC} in the FT promptly declined
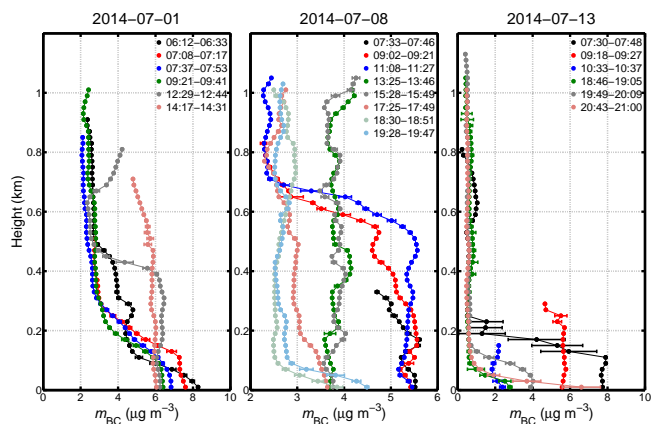
Figure 6. Vertical distributions of BC separately displayed for 1, 8, and 13 July. Profiles collected at different time are shown in different colors. As in Fig. 4, dots represent 20 m averaged m_{BC}, with standard deviations given in error bars.

Figure 7. (a) H_m identified from BC vertical profiles in the selected dataset. Measurements made on different days are marked by dots in different colors. H_m from the ascent and descent of one launch are connected by black lines. (b) Average m_{BC} within the ML (C_m) during the daytime (before 18:00 LT) are marked by solid dots. Average m_{BC} within 20 m near the surface in the evening are marked by open dots.

to its typical level, often leaving no trail to indicate the daytime mixing with polluted air masses beneath. In contrast, air pollutants including BC quickly built up in the shallow NBL. Sometimes, a residual layer with a relatively high level of m_{BC} ($> 2\,\mu g\,m^{-3}$) could be formed above the NBL where the remnant of the daytime mixing layer might be traced after its collapse (e.g., profiles on 8 July). This would undoubtedly have an impact on measured m_{BC} above the mixing layer the next day, leading to a polluted background in the FT (e.g., in the morning of 1 and 8 July). The role of the residual layer in affecting the evolution of the PBL still stays controversial, though it has been established that BC could heat the PBL and intensify atmospheric stability. Ding et al. (2016) demonstrated the importance of the "dome effect" of BC in the PBL, especially the upper PBL, suppressing the PBL height and enhancing haze pollution within a lower PBL, whereas in Zhang et al. (2012), a limited warming effect of BC in an elevated aerosol layer and a limited induced increase in the strength of atmospheric inversion were indicated.

It was interestingly noticed that a polluted layer with a thickness of about 0.3 km, extending from the height of 0.2 to 0.5 km, lay right above the ML in the early morning on 1 July. The polluted layer could also be accordingly recognized from meteorological features of more moisture and wind shear across its boundaries. Wind direction was southeast in the ML and the FT, while it was southwest in the polluted layer. Average m_{BC} within the polluted layer was about $4\,\mu g\,m^{-3}$, half of that near the surface and double of that in the FT. Actually, the vertical profile within the morning ML quite resembled characteristics of a nocturnal profile even though the sun had risen, suggesting that strong inversion of the NBL still overrode weak vertical turbulence at that time. As surface emissions from human activities kept increasing, m_{BC} within the ML was elevated. Further development of vertical convection b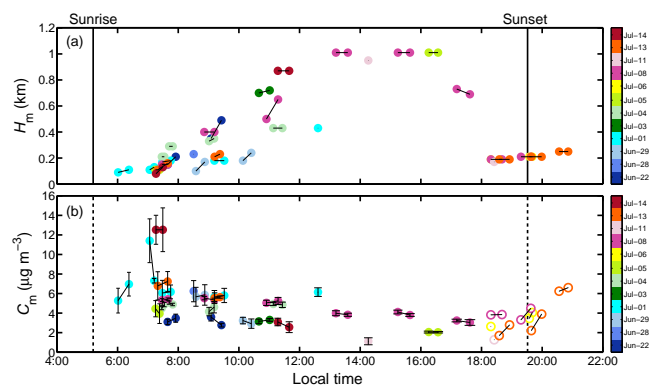roke the layered structure, leading to the merge of the polluted layer and the ML. Slowly, the polluted layer vanished into the convective ML, though it remained until 09:00 LT in the morning. An elevated aerosol layer (0.7–1 km), in which BC was well aged, has previously been observed in the afternoon over Beijing by Zhang et al. (2012), and was attributed to the residual nocturnal stable layer. Possible origin of the polluted layer present here and the status of BC in the layer were unable to be decided on the basis of limited observations. Nonetheless, a higher q in the polluted layer than at the surface and different wind direction might imply an elevated residual layer formed after sunset the day before and transported from somewhere else. It was quite cloudy and sultry during the daytime, and a heavy rainfall occurred near the evening. Thus, the top of the ML was still below 0.5 km when the launch was carried out around noon. Despite the fact that the tethered balloon failed to reach 1 km due to strong winds aloft, a part of a relatively polluted layer with apparent increase in moisture and potential temperature could be roughly distinguished. Wind direction in the polluted layer was southwest, whereas predominant wind direction beneath had changed to southeast. The polluted layer, extending from about 0.7 km to the top of the reachable height, disappeared during the last launch around 14:00 LT on that day and was probably a transported plume.

Figure 7 displays H_m and m_{BC} from the entire selected dataset on a diurnal scale. Observations on each day are shown in one color. Variations in H_m through the field campaign generally resembled the diurnal cycle observed on an individual day (Fig. 7a). The ML, though still shallow, developed slowly after sunrise. In addition to a high level of BC trapped near the ground by the stable NBL, fresh emissions from daytime human activities further aggravated sur-

Table 3. Measurements of BC vertical distributions in different regions. m_{BC} is the range and/or average value $\pm$ standard deviation of BC mass concentrations, depending upon what is available in the literature. Height specifies how m_{BC} is obtained.

Locations	Type	Period	Method	m_{BC} ($\mu g\,m^{-3}$)	Height	References
Los Angeles Basin, USA	Mixture	May 2010	Aircraft, SP2*	0.01–0.53	0.3 km	Metcalf et al. (2012)
				0.03 $\pm$ 0.05	FT	
Milan, Italy	Urban	Feb. 2010	Tethered balloon, AE-51	7.57 $\pm$ 1.28	ML	Ferrero et al. (2014)
				2.03 $\pm$ 0.34	FT	
Multi-cities, India	Urban	Jun. 2005	Aircraft, AE-42, AE-21	1.50–7.50	PBL	Safai et al. (2012) and references therein
Beijing, China	Urban	May–Jun. 2012	Aircraft, SP2	0.24–4.02	PBL	Zhao et al. (2015)
Shanghai, China	Urban	Dec. 2013	Tethered balloon, AE-31	3.20–7.30	0–1 km	Li et al. (2015)
Central NCP, China	Semirural	Jun.–Jul. 2014	Tethered balloon, AE-51	1.12–14.49 (5.16 $\pm$ 2.49)	ML	This study
				0.36–3.14 (1.61 $\pm$ 0.94)	FT	

* SP2: Single Particle Soot Photometer.

face pollution. Observed m_{BC} was usually quite high in the early morning, and sometimes even experienced an increase with time, depending upon how fast the ML developed and emissions increased. The thickening of the mixing depth accelerated in the late morning on sunny days, whereas it slowed down on cloudy days, only forming a thin mixing layer. Accordingly, C_m (solid dots in Fig. 7b) largely reduced from morning to noon in the strongly convective ML on sunny days; however, it stayed relatively stable through the morning on cloudy days. Comparative cases could be found on 1 and 14 July. Based on current knowledge of the boundary layer, the maximum height of the ML on sunny days would be reached in the late afternoon, but could not be observed in this study since it was well above the flight limit of the tethered balloon. The collapse of the ML was not directly captured. However, intensive measurements favored by the meteorology on 8 July revealed that the convective ML quickly faded away on a timescale of 1 h near sunset. Instead, a stable and shallow NBL confined nighttime emissions near the ground, giving rise to enhanced surface pollution (open dots in Fig. 7b).

4 Conclusions

In situ measurements of black carbon (BC) vertical profiles were carried out at a semirural site during the VOGA 2014 summer field campaign, using a micro-aethalometer attached to a tethered balloon system. A set of 67 BC vertical profiles was reliably collected and diurnal variations of BC vertical profiles were examined.

Vertical distributions of BC and meteorological parameters, as well as the mixing height (H_m) identified from BC profiles, experienced a distinct diurnal cycle guided by the development of the mixing layer (ML). In the morning, weak turbulence within the shallow ML (thinner than 0.2 km) favored the accumulation of enhanced surface emis-

sions, sometimes leading to severe pollution with BC mass concentrations (m_{BC}) exceeding $10\,\mu g\,m^{-3}$. The high level of BC within the ML was diluted with the fast development of a strongly convective ML. H_m reached its maximum in the late afternoon and exceeded 1 km on sunny days, whereas it stayed much lower on cloudy days. Typically in the daytime, BC was uniformly distributed within the ML and sharply decreased above the ML to a level even less than 10 % of that near the surface. Average m_{BC} within the ML (C_m) was about $5.16 \pm 2.49\,\mu g\,m^{-3}$ over the entire field campaign, with a range of 1.12 to $14.49\,\mu g\,m^{-3}$, comparable with what has been observed in many polluted urban areas. C_f, average m_{BC} in the free troposphere (FT), was below $1\,\mu g\,m^{-3}$ under clean conditions and amounted to half of the ground level under pollution conditions. In the evening, BC quickly built up near the surface and exponentially declined with height, following the collapse of the ML and the formation of a stable nocturnal boundary layer (NBL). Particularly, two polluted layers were observed at different times and heights on 1 July. Origins of the polluted layers were not able to be evidently decided. However, the presence of BC polluted layers in the FT, either as an elevated residual layer in the morning or a transported plume in the afternoon, as suggested by the history of the layer and the meteorology, might considerably influence direct radiative forcing by BC and atmospheric stability.

5 Data availability

All vertical profiles presented in this paper and the code for the FMS algorithm can be accessed by contacting corresponding authors, Liang Ran (shirleyrl@mail.iap.ac.cn) and Zhaoze Deng (dengzz@mail.iap.ac.cn).

Appendix A: Nomenclature

Symbol	Definition
α	Aerosol absorption Ångström exponent, calculated here from $\sigma_{\text{AE-31, 660 nm}}$ and $\sigma_{\text{AE-31, 880 nm}}$
$\sigma_{\text{AE-31, 660 nm}}$	Aerosol absorption coefficient measured by AE-31 at the wavelength of 660 nm
$\sigma_{\text{AE-31, 880 nm}}$	Aerosol absorption coefficient measured by AE-31 at the wavelength of 880 nm
$\sigma_{\text{MAAP, 637 nm}}$	Aerosol absorption coefficient measured by MAAP at the wavelength of 637 nm
$\sigma_{\text{MAAP, 880 nm}}$	Aerosol absorption coefficient at the wavelength of 880 nm, calculated from α and $\sigma_{\text{MAAP, 637 nm}}$
$\sigma_{\text{AE-51, 880 nm}}$	Aerosol absorption coefficient measured by AE-51 at the wavelength of 880 nm
σ_{BC}	Absorption coefficient of black carbon at the wavelength of 880 nm
λ	Wavelength
θ	Potential temperature
ATN	Light attenuation
C	Correction factor for filter multiple scattering and aerosol scattering
C_f	Average m_{BC} in the free troposphere
C_m	Average m_{BC} within the mixing layer
C_{fs}	Characteristic m_{BC} in the free troposphere, derived from sigmoid fitting
C_{ms}	Characteristic m_{BC} within the mixing layer, derived from sigmoid fitting
H_e	The thickness of the entrainment layer, derived from sigmoid fitting
H_m	The height of the mixing layer, also used to denote the height of the NBL layer in this study
$H_{\text{m, BC, gradient}}$	The height of the mixing layer estimated from the vertical profile of BC using the gradient method
$H_{\text{m, BC, sigmoid}}$	The height of the mixing layer estimated from the vertical profile of BC using the sigmoid function
$H_{\text{m},\theta}$	The height of the mixing layer estimated from the vertical profile of θ using the gradient method
$H_{\text{m},q}$	The height of the mixing layer estimated from the vertical profile of q using the gradient method
H_{Nor}	The normalized height, defined as $h/H_m - 1$
m_{BC}	Mass concentration of black carbon, converted from $\sigma_{\text{AE-51, 880 nm}}$
q	Specific humidity
RH	Relative humidity
T	Temperature

References

Andreae, M. O.: The dark side of aerosols, Nature, 409, 671–672, 2001.

Arnott, W. P., Hamasha, K., Moosmuller, H., Sheridan P. J., and Ogren J. A.: Towards aerosol light-absorption measurements with a 7-wavelength aethalometer: evaluation with a photoacoustic instrument and 3-wavelength nephelometer, Aerosol Sci. Tech., 39, 17–29, doi:10.1080/027868290901972, 2005.

Babu, S. S., Sreekanth, V., Moorthy, K. K., Mohan, M., Kirankumar, N. V. P., Subrahamanyam, D. B., Gogoi, M. M., Kompalli, S. K., Beegum, N., Chaubey, J. P., Kumar, V. H. A., and Manchanda, R. K.: Vertical profiles of aerosol black carbon in the atmospheric boundary layer over a tropical coastal station: Perturbations during an annular solar eclipse, Atmos. Res., 99, 471–478, doi:10.1016/j.atmosres.2010.11.019, 2011a.

Babu, S. S., Moorthy, K. K., Manchanda, R. K., Sinha, P. R., Satheesh, S. K., Vajja, D. P., Srinivasan, S., and Kumar, V. H. A.: Free tropospheric black carbon aerosol measurements using high altitude balloon: Do BC layers build "their own homes" up in the atmosphere?, Geophys. Res. Lett., 38, L08803, doi:10.1029/2011GL046654, 2011b.

Ban-Weiss, G. A., Cao, L., Bala, G., and Caldeira, K.: Dependence of climate forcing and response on the altitude of black carbon aerosols, Clim. Dynam., 38, 897–911, doi:10.1007/s00382-011-1052-y, 2012.

Bond, T. C., Habib, G., and Bergstrom, R. W.: Limitations in the enhancement of visible light absorption due to mixing state, J. Geophys. Res., 111, D20211, doi:10.1029/2006JD007315, 2006.

Bond, T. C., Doherty, S. J., Fahey, D. W., Forster, P. M., Berntsen, T., DeAngelo, B. J., Flanner, M. G., Ghan, S., Kärcher, B., Koch, D., Kinne, S., Kondo, Y., Quinn, P. K., Sarofim, M. C., Schultz, M. G., Schulz, M., Venkataraman, C., Zhang, H., Zhang, S., Bellouin, N., Guttikunda, S. K., Hopke, P. K., Jacobson, M. Z., Kaiser, J. W., Klimont, Z., Lohmann, U., Schwarz, J. P., Shindell, D., Storelvmo, T., Warren, S. G., and Zender, C. S.: Bounding the role of black carbon in the climate system: a scientific assessment, J. Geophys. Res., 118, 5380–5552, doi:10.1002/jgrd.50171, 2013.

Chen, J., Zhao, C. S., Ma, N., Liu, P. F., Göbel, T., Hallbauer, E., Deng, Z. Z., Ran, L., Xu, W. Y., Liang, Z., Liu, H. J., Yan, P., Zhou, X. J., and Wiedensohler, A.: A parameterization of low visibilities for hazy days in the North China Plain, Atmos. Chem. Phys., 12, 4935–4950, doi:10.5194/acp-12-4935-2012, 2012.

Collaud Coen, M., Weingartner, E., Apituley, A., Ceburnis, D., Fierz-Schmidhauser, R., Flentje, H., Henzing, J. S., Jennings, S. G., Moerman, M., Petzold, A., Schmid, O., and Baltensperger, U.: Minimizing light absorption measurement artifacts of the Aethalometer: evaluation of five correction algorithms, Atmos. Meas. Tech., 3, 457–474, doi:10.5194/amt-3-457-2010, 2010.

Corrigan, C. E., Roberts, G. C., Ramana, M. V., Kim, D., and Ramanathan, V.: Capturing vertical profiles of aerosols and black carbon over the Indian Ocean using autonomous unmanned aerial vehicles, Atmos. Chem. Phys., 8, 737–747, doi:10.5194/acp-8-737-2008, 2008.

Ding, A. J., Huang, X., Nie, W., Sun, N. J., Kerminen, V. M., Petäjä, T., Su, H., Cheng, Y. F., Yang, X. Q., Wang, M. H., Chi, X. G., Wang, J. P., Virkkula, A., Guo, W. D., Yuan, J., Wang, S. Y., Zhang, R. J. Zhang, Wu, Y. F., Song, Y. Song, Zhu, T., Zilitinkevich, S., Kulmala, M., and Fu, C. B.: Enhanced haze pollution by black carbon in megacities in China, Geophys. Res. Lett., 43, 2873–2879, doi:10.1002/2016GL067745, 2016.

Ferrero, L., Perrone, M. G., Petraccone, S., Sangiorgi, G., Ferrini, B. S., Lo Porto, C., Lazzati, Z., Cocchi, D., Bruno, F., Greco, F., Riccio, A., and Bolzacchini, E.: Vertically-resolved particle size distribution within and above the mixing layer over the Milan metropolitan area, Atmos. Chem. Phys., 10, 3915–3932, doi:10.5194/acp-10-3915-2010, 2010.

Ferrero, L., Mocnik, G., Ferrini, B. S., Perrone, M. G., Sangiorgi, G., and Bolzacchini, E.: Vertical profiles of aerosol absorption coefficient from micro-aethalometer data and Mie calculation over Milan, Sci. Total Environ., 40, 2824–2837, doi:10.1016/j.scitotenv.2011.04.022, 2011a.

Ferrero, L., Riccio, A., Perrone, M. G., Sangiorgi, G., Ferrini, B. S., and Bolzacchini, E.: Mixing height determination by tethered balloon-based particle soundings and modeling simulations, Atmos. Res., 102, 145–156, doi:10.1016/j.atmosres.2011.06.016, 2011b.

Ferrero, L., Castelli, M., Ferrini, B. S., Moscatelli, M., Perrone, M. G., Sangiorgi, G., D'Angelo, L., Rovelli, G., Moroni, B., Scardazza, F., Mocnik, G., Bolzacchini, E., Petitta, M., and Cappelletti, D.: Impact of black carbon aerosol over Italian basin valleys: high-resolution measurements along vertical profiles, radiative forcing and heating rate, Atmos. Chem. Phys., 14, 9641–9664, doi:10.5194/acp-14-9641-2014, 2014.

Hagler, G. S. W., Yelverton, T. L. B., Vedantham, R., Hansen, A. D. A., and Turner, J. R.: Post-Processing Method to Reduce Noise while Preserving High Time Resolution in Aethalometer Real-Time Black Carbon Data, Aerosol Air Qual. Res., 11, 539–546, doi:10.4209/aaqr.2011.05.0055, 2011.

Hansen, A. D. A., Rosen, H., and Novakov, T.: The aethalometer - an instrument for the real-time measurement of optical absorption by aerosol particles, Sci. Total Environ., 36, 191–196, 1984.

Höpner, F., Bender, F. A.-M., Ekman, A. M. L., Praveen, P. S., Bosch, C., Ogren, J. A., Andersson, A., Gustafsson, Ö., and Ramanathan, V.: Vertical profiles of optical and microphysical particle properties above the northern Indian Ocean during CARDEX 2012, Atmos. Chem. Phys., 16, 1045–1064, doi:10.5194/acp-16-1045-2016, 2016.

Hyvärinen, A.-P., Vakkari, V., Laakso, L., Hooda, R. K., Sharma, V. P., Panwar, T. S., Beukes, J. P., van Zyl, P. G., Josipovic, M., Garland, R. M., Andreae, M. O., Pöschl, U., and Petzold, A.: Correction for a measurement artifact of the Multi-Angle Absorption Photometer (MAAP) at high black carbon mass concentration levels, Atmos. Meas. Tech., 6, 81–90, doi:10.5194/amt-6-81-2013, 2013.

IPCC: Summary for policymakers, Climate change 2013: the physical science basis, Cambridge University Press, Cambridge, UK and New York, NY, USA, 2216 pp., 2013.

Jacobson, M. Z.: Strong radiative heating due to the mixing state of black carbon in atmospheric aerosols, Nature, 409, 695–697, 2001.

Janssen, N. A., Gerlofs-Nijland, M. E., Lanki, T., Salonen, R. O., Cassee, F., Hoek, G., Fischer, P., Brunekreef, B., and Krzyzanowski, M.: Health effects of black carbon, World Health Organization, Copenhagen, 2012.

Kaimal, J. C. and Finnigan, J. J.: Atmospheric boundary layer flows: their structure and measurement, Oxford University Press, New York, 289 pp., 1994.

Kim, S. W., Yoon, S. C., Won, J. G., and Choi, S. C.: Ground-based remote sensing measurements of aerosol and ozone in an urban area: a case study of mixing height evolution and its effect on ground-level ozone concentrations, Atmos. Environ., 41, 7069-7081, doi:10.1016/j.atmosenv.2007.04.063, 2007.

Lazaridis, M.: First principles of meteorology and air pollution, Environ. Poll., Springer, the Netherlands, 362 pp., 2011.

Lei, Y., Zhang, Q., He, K. B., and Streets, D. G.: Primary anthropogenic aerosol emission trends for China, 1990–2005, Atmos. Chem. Phys., 11, 931–954, doi:10.5194/acp-11-931-2011, 2011.

Levy, R. and Hsu, C.: MODIS Atmosphere L2 Aerosol Product, NASA MODIS Adaptive Processing System, Goddard Space Flight Center, USA, doi:10.5067/MODIS/MYD04_L2.006, 2015.

Li, J., Fu, Q. Y., Huo, J. T., Wang, D. F., Yang, W., Bian, Q. G., Duan, Y. S., Zhang, Y. H., Pan, J., Lin, Y. F., Huang, K., Bai, Z. P., Wang, S. H., Fu, J. S., and Louie, P. K. K.: Tethered balloon-based black carbon profiles within the lower troposphere of Shanghai in the 2013 East China smog, Atmos. Environ., 123, 327–338, doi:10.1016/j.atmosenv.2015.08.096, 2015.

Li, M., Zhang, Q., Kurokawa, J., Woo, J.-H., He, K. B., Lu, Z., Ohara, T., Song, Y., Streets, D. G., Carmichael, G. R., Cheng, Y. F., Hong, C. P., Huo, H., Jiang, X. J., Kang, S. C., Liu, F., Su, H., and Zheng, B.: MIX: a mosaic Asian anthropogenic emission inventory for the MICS-Asia and the HTAP projects, Atmos. Chem. Phys. Discuss., 15, 34813–34869, doi:10.5194/acpd-15-34813-2015, 2015.

Liao, H. and Shang, J. J.: Regional warming by black carbon and tropospheric ozone: a review of progresses and research challenges in China, J. Meteor. Res., 29, 525–545, doi:10.1007/s13351-015-4120-0, 2015.

Ma, N., Zhao, C. S., Nowak, A., Müller, T., Pfeifer, S., Cheng, Y. F., Deng, Z. Z., Liu, P. F., Xu, W. Y., Ran, L., Yan, P., Göbel,

T., Hallbauer, E., Mildenberger, K., Henning, S., Yu, J., Chen, L. L., Zhou, X. J., Stratmann, F., and Wiedensohler, A.: Aerosol optical properties in the North China Plain during HaChi campaign: an in-situ optical closure study, Atmos. Chem. Phys., 11, 5959–5973, doi:10.5194/acp-11-5959-2011, 2011.

Menon, S., Hansen, J., Nazarenko, L., and Luo, Y. F.: Climate effects of black carbon aerosols in China and India, Science, 297, 2250–2253, doi:10.1126/science.1075159, 2002.

Metcalf, A. R., Craven, J. S., Ensberg, J. J., Brioude, J., Angevine, W., Sorooshian, A., Duong, H. T., Jonsson, H. H., Flagan, R. C., and Seinfeld, J. H.: Black carbon aerosol over the Los Angeles Basin during CalNex, J. Geophys. Res., 117, D00V13, doi:10.1029/2011JD017255, 2012.

Miffre, A., Anselmo, C., Geffroy, S., Frejafon, E., and Rairoux, P.: Lidar remote sensing of laser-induced incandescence on light absorbing particles in the atmosphere, Opt. Express, 23, 2347–2360, doi:10.1364/OE.23.002347, 2015.

Moosmüller, H., Chakrabarty, R. K., and Arnott, W. P.: Aerosol light absorption and its measurement: a review, J. Quant. Spectrosc. Ra., 110, 844–878, doi:10.1016/j.jqsrt.2009.02.035, 2009.

Müller, T., Henzing, J. S., de Leeuw, G., Wiedensohler, A., Alastuey, A., Angelov, H., Bizjak, M., Collaud Coen, M., Engström, J. E., Gruening, C., Hillamo, R., Hoffer, A., Imre, K., Ivanow, P., Jennings, G., Sun, J. Y., Kalivitis, N., Karlsson, H., Komppula, M., Laj, P., Li, S.-M., Lunder, C., Marinoni, A., Martins dos Santos, S., Moerman, M., Nowak, A., Ogren, J. A., Petzold, A., Pichon, J. M., Rodriquez, S., Sharma, S., Sheridan, P. J., Teinilä, K., Tuch, T., Viana, M., Virkkula, A., Weingartner, E., Wilhelm, R., and Wang, Y. Q.: Characterization and intercomparison of aerosol absorption photometers: result of two intercomparison workshops, Atmos. Meas. Tech., 4, 245–268, doi:10.5194/amt-4-245-2011, 2011.

Nichols, J. L., Owens, E. O., Dutton, S. J., and Luben, T. J.: Systematic review of the effects of black carbon on cardiovascular, Int. J. Public Health, 58, 707–724, doi:10.1007/s00038-013-0492-z, 2013.

Petzold, A. and Schönlinner, M.: Multi-angle absorption photometry – a new method for the measurement of aerosol light absorption and atmospheric black carbon, J. Aerosol Sci., 35, 421–441, doi:10.1016/j.jaerosci.2003.09.005, 2004.

Petzold, A., Schloesser, H., Sheridan, P. J., Arnott, W. P., Ogren, J. A., and Virkkula, A.: Evaluation of multiangle absorption photometry for measuring aerosol light absorption, Aerosol Sci. Tech., 39, 40–51, doi:10.1080/027868290901945, 2005.

Poulos, G. S., Blumen, W., Fritts, D. C., Lundquist, J. K., Sun, J. L., Burns, S. P., Nappo, C., Banta, R., Newsom, R., Cuxart, J., Terrandellas, E., Balsley, B., and Jensen, M.: CASES-99: a comprehensive investigation of the stable nocturnal boundary layer, B. Am. Meteorol. Soc., 83, 555–581, 2002.

Ramachandran, S. and Rajesh, T. A.: Black carbon aerosol mass concentrations over Ahmedabad, an urban location in western India: comparison with urban sites in Asia, Europe, Canada, and the United States, J. Geophys. Res., 112, D06211, doi:10.1029/2006JD007488, 2007.

Ramanathan, V. and Carmichael, G.: Global and regional climate changes due to black carbon, Nat. Geosci., 1, 221–227, 2008.

Ramanathan, V., Chung, C., Kim, D., Bettge, T., Buja, L., Kiehl, J. T., Washington, W. M., Fu, Q., Sikka, D. R., and Wild, M.: Atmospheric brown clouds: impacts on South Asian climate and

hydrological cycle, P. Natl. Acad. Sci. USA, 102, 5326–5333, doi:10.1073/pnas.0500656102, 2005.

Ran, L., Deng, Z. Z., Wang, P. C., and Xia, X. A.: Black carbon and wavelength-dependent aerosol absorption in the North China Plain based on two-year aethalometer measurements, Atmos. Environ., 142, 132–144, doi:10.1016/j.atmosenv.2016.07.014, 2016.

Ryerson, T. B., Andrews, A. E., Angevine, W. M., Bates, T. S., Brock, C. A., Cairns, B., Cohen, R. C., Cooper, O. R., de Gouw, J. A., Fehsenfeld, F. C., Ferrare, R. A., Fischer, M. L., Flagan, R. C., Goldstein, A. H., Hair, J. W., Hardesty, R. M., Hostetler, C. A., Jimenez, J. L., Langford, A. O., McCauley, E., McKeen, S. A., Molina, L. T., Nenes, A., Oltmans, S. J., Parrish, D. D., Pederson, J. R., Pierce, R. B., Prather, K., Quinn, P. K., Seinfeld, J. H., Senff, C. J., Sorooshian, A., Stutz, J., Surratt, J. D., Trainer, M., Volkamer, R., Williams, E. J., and Wofsy, S. C.: The 2010 California Research at the Nexus of Air Quality and Climate Change (CalNex) field study, J. Geophys. Res., 118, 5830–5866, doi:10.1002/jgrd.50331, 2013.

Safai, P. D., Raju, M. P., Maheshkumar, R. S., Kulkarni, J. R., Rao, P. S. P., and Devara, P. C. S.: Vertical profiles of black carbon aerosols over the urban locations in South India, Sci. Total Environ., 431, 323–331, doi:10.1016/j.scitotenv.2012.05.058, 2012.

Samset, B. H., Myhre, G., Schulz, M., Balkanski, Y., Bauer, S., Berntsen, T. K., Bian, H., Bellouin, N., Diehl, T., Easter, R. C., Ghan, S. J., Iversen, T., Kinne, S., Kirkevåg, A., Lamarque, J.-F., Lin, G., Liu, X., Penner, J. E., Seland, Ø., Skeie, R. B., Stier, P., Takemura, T., Tsigaridis, K., and Zhang, K.: Black carbon vertical profiles strongly affect its radiative forcing uncertainty, Atmos. Chem. Phys., 13, 2423–2434, doi:10.5194/acp-13-2423-2013, 2013.

Sandradewi, J., Prevot, A. S. H., Weingartner, E., Schmidhauser, R., Gysel, M., and Baltensperger, U.: A study of wood burning and traffic aerosols in an Alpine valley using a multi-wavelength aethalometer, Atmos. Environ., 42, 101–112, doi:10.1016/j.atmosenv.2007.09.034, 2008.

Schmid, O., Artaxo, P., Arnott, W. P., Chand, D., Gatti, L. V., Frank, G. P., Hoffer, A., Schnaiter, M., and Andreae, M. O.: Spectral light absorption by ambient aerosols influenced by biomass burning in the Amazon Basin. I: Comparison and field calibration of absorption measurement techniques, Atmos. Chem. Phys., 6, 3443–3462, doi:10.5194/acp-6-3443-2006, 2006.

Seibert, P., Beyrich, F., Gryning, S. E., Joffre, S., Rasmussen, A., and Tercier, P.: Review and intercomparison of operational methods for the determination of the mixing height, Atmos. Environ., 34, 1001–1027, doi:10.1016/S1352-2310(99)00349-0, 2000.

Shao, M., Tang, X. Y., Zhang, Y. H., and Li, W. J.: City clusters in China: air and surface water pollution, Front. Ecol. Environ., 4, 353–361, doi:10.1890/1540-9295(2006)004[0353:CCICAA]2.0.CO;2, 2006.

Stier, P., Seinfeld, J. H., Kinne, S., and Boucher, O.: Aerosol absorption and radiative forcing, Atmos. Chem. Phys., 7, 5237–5261, doi:10.5194/acp-7-5237-2007, 2007.

Streets, D. G., Gupta, S., Waldhoff, S. T., Wang, M. Q., Bond, T. C., and Bo, Y. Y.: Black carbon emissions in China, Atmos. Environ., 35, 4281–4296, doi:10.1016/S1352-2310(01)00179-0, 2001.

Tripathi, S. N., Dey, S., Satheesh, S. K., Lal, S., and Venkataramani, S.: Enhanced layer of black carbon in a north Indian industrial Indian city, Geophys. Res. Lett., 32, L12802, doi:10.1029/2005GL022564, 2005.

Tripathi, S. N., Srivastava, A. K., Dey, S., Satheesh, S. K., and Krishnamoorthy, K.: The vertical profile off atmospheric heating rate of black carbon aerosols at Kanpur in northern India, Atmos. Environ., 41, 6909–6915, doi:10.1016/j.atmosenv.2007.06.032, 2007.

Virkkula, A., Mäkelä, T., Hillamo, R., Yli-Tuomi, T., Hirsikko, A., Hämeri, K., and Koponen, I. K.: A simple procedure for correcting loading effects of aethalometer data, J. Air Waste Manage., 57, 1214–1222, doi:10.3155/1047-3289.57.10.1214, 2007.

Weingartner, E., Saathoff, H., Schnaiter, M., Streit, N., Bitnar, B., and Baltensperger, U.: Absorption of light by soot particles: determination of the absorption coefficient by means of aethalometers, J. Aerosol Sci., 34, 1445–1463, doi:10.1016/S0021-8502(03)00359-8, 2003.

Xu, W. Y., Zhao, C. S., Ran, L., Deng, Z. Z., Liu, P. F., Ma, N., Lin, W. L., Xu, X. B., Yan, P., He, X., Yu, J., Liang, W. D., and Chen, L. L.: Characteristics of pollutants and their correlation to meteorological conditions at a suburban site in the North China Plain, Atmos. Chem. Phys., 11, 4353-4369, doi:10.5194/acp-11-4353-2011, 2011.

Yu, H. B., Liu, S. C., and Dickinson, R. E.: Radiative effects of aerosols on the evolution of the atmospheric boundary layer, J. Geophys. Res., 107, 4142, doi:10.1029/2001JD000754, 2002.

Yu, T. W.: Determining height of the nocturnal boundary layer, J. Appl. Meteorol., 17, 28–33, 1978.

Zarzycki, C. M. and Bond, T. C.: How much can the vertical distribution of black carbon affect its global direct radiative forcing?, Geophys. Res. Lett., 37, L20807, doi:10.1029/2010gl044555, 2010.

Zhang, D. Z., Chen, B., Yamada, M., Niu, H. Y., Wang, B., Iwasaka, Y., and Shi, G. Y.: Elevated soot layer in polluted urban atmosphere: a case study in Beijing, J. Meteorol. Soc. Japn., 90, 361–375, doi:10.2151/jmsj.2012-302, 2012.

Zhang, X., Tang, J., Wu, Y. F., Wu, J., Yan, P., and Zhang, R. J.: Variations of black carbon aerosol observed in Beijing and surrounding area during 2006–2012, China Powder Sci. Tech., 21, 24–35, doi:10.13732/j.issn.1008-5548.2015.04.006, 2015.

Zhao, D. L., Tie, X. X., Gao, Y., Zhang, Q., Tan, H. J., Bi, K., Jin, Y. L., and Chen, P. F.: In-situ aircraft measurements of the vertical distribution of black carbon in the lower troposphere of Beijing, China, in the Spring and Summer Time, Atmosphere, 6, 713–731, doi:10.3390/atmos6050713, 2015.